Published in final edited form as:

Adv Mater. 2018 March ; 30(13): e1705799. doi:10.1002/adma.201705799.

3D NIR-II Molecular Imaging Distinguishes Targeted Organs with High-Performance NIR-II Bioconjugates

Dr Shoujun Zhu,
Department of Chemistry, Stanford University, Stanford, CA 94305, USA

Dr Sonia Herraiz,
Program of Reproductive and Stem Cell Biology, Department of Obstetrics and Gynecology, Stanford University School of Medicine, Stanford, CA 94305, USA

IVI Foundation, Valencia 46026, Spain

Jingying Yue,
Department of Chemistry, Stanford University, Stanford, CA 94305, USA

Dr Mingxi Zhang,
Department of Chemistry, Stanford University, Stanford, CA 94305, USA

Dr Hao Wan,
Department of Chemistry, Stanford University, Stanford, CA 94305, USA

Department of Materials Science & Engineering, South University of Science & Technology of China, Shenzhen 518055, China

Dr Qinglai Yang,
Department of Materials Science & Engineering, South University of Science & Technology of China, Shenzhen 518055, China

Research Center for Advanced Materials and Biotechnology, Research Institute of Tsinghua University in Shenzhen, Shenzhen 518057, China

Zhuoran Ma,
Department of Chemistry, Stanford University, Stanford, CA 94305, USA

Dr Yan Wang,
Program of Reproductive and Stem Cell Biology, Department of Obstetrics and Gynecology, Stanford University School of Medicine, Stanford, CA 94305, USA

Jiahuan He,
Program of Reproductive and Stem Cell Biology, Department of Obstetrics and Gynecology, Stanford University School of Medicine, Stanford, CA 94305, USA

Correspondence to: Yongye Liang; Aaron J. Hsueh; Hongjie Dai.

S.Z., S.H., J.Y., M.Z., H.W. contributed equally to this work.

Supporting Information

Supporting Information is available from the Wiley Online Library or from the author.

Conflict of Interest

The authors declare no conflict of interest.

Dr Alexander L. Antaris,
Department of Chemistry, Stanford University, Stanford, CA 94305, USA

Dr Yeteng Zhong,
Department of Chemistry, Stanford University, Stanford, CA 94305, USA

Dr Shuo Diao,
Department of Chemistry, Stanford University, Stanford, CA 94305, USA

Dr Yi Feng,
Program of Reproductive and Stem Cell Biology, Department of Obstetrics and Gynecology, Stanford University School of Medicine, Stanford, CA 94305, USA

Ying Zhou,
Department of Chemistry, Stanford University, Stanford, CA 94305, USA

Dr Kuai Yu,
Department of Chemistry, Stanford University, Stanford, CA 94305, USA

Dr Guosong Hong,
Department of Chemistry, Stanford University, Stanford, CA 94305, USA

Prof Yongye Liang,
Department of Materials Science & Engineering, South University of Science & Technology of China, Shenzhen 518055, China

Prof Aaron J. Hsueh, and
Program of Reproductive and Stem Cell Biology, Department of Obstetrics and Gynecology, Stanford University School of Medicine, Stanford, CA 94305, USA

Prof Hongjie Dai
Department of Chemistry, Stanford University, Stanford, CA 94305, USA

Abstract

Greatly reduced scattering in the second near-infrared (NIR-II) region (1000–1700 nm) opens up many new exciting avenues of bioimaging research, yet NIR-II fluorescence imaging is mostly implemented by using nontargeted fluorophores or wide-field imaging setups, limiting the signal-to-background ratio and imaging penetration depth due to poor specific binding and out-of-focus signals. A newly developed high-performance NIR-II bioconjugate enables targeted imaging of a specific organ in the living body with high quality. Combined with a home-built NIR-II confocal set-up, the enhanced imaging technique allows 900 μm-deep 3D organ imaging without tissue clearing techniques. Bioconjugation of two hormones to nonoverlapping NIR-II fluorophores facilitates two-color imaging of different receptors, demonstrating unprecedented multicolor live molecular imaging across the NIR-II window. This deep tissue imaging of specific receptors in live animals allows development of noninvasive molecular imaging of multifarious models of normal and neoplastic organs in vivo, beyond the traditional visible to NIR-I range. The developed NIR-II fluorescence microscopy will become a powerful imaging technique for deep tissue imaging without any physical sectioning or clearing treatment of the tissue.

Keywords

3D NIR-II molecular imaging; high-performance NIR-II bioconjugate; live ovary imaging; multicolor live molecular imaging; NIR-II confocal

NIR-II biomedical fluorescence imaging in the 1000–1700 nm “second near-infrared (NIR-II) window” allows researchers and clinicians to peer deeper into the body with a higher degree of clarity compared to previous one-photofluorescence imaging modalities, owing to both reduced photon scattering and tissue autofluorescence when imaging at progressively longer wave-lengths. Recent advances in in vivo fluorescence imaging of biological systems in the NIR-II window reached deeper into tissues, improved spatial resolution and facilitated a number of preclinical imaging studies.[1–9] Thus far most works on NIR-II fluorescence imaging relied on wide-field imaging to capture 2D projected[10,11] epifluorescence photographs without 3D volumetric information.[12–14] The foreground fluorescence signal out of focus in an epifluorescence scheme superimposes onto the in-focus signal of interest, usually blurs the image and limits the penetration depth of the imaging.

To circumvent the problem of strong tissue scattering of light, physical sectioning[15] and optical clearing techniques[16,17] have been used to treat large volumes of tissues to avoid scattering and absorption of fluorescence photons. Although one can achieve 3D reconstruction of millimeter-thick samples based on fluorescence imaging with these treatments,[16] these techniques are limited to ex vivo tissue samples and not applicable to live animals.

Currently, NIR-II fluorescent agents include a number of molecular dyes and inorganic nanomaterials.[18–20] For NIR-II molecular imaging at deep tissues with long-wavelength fluorescence, the development of highly specific NIR-II molecular imaging probes is needed. It is well known that diverse peptide hormones act on their specific plasma membrane receptors in target cells to regulate unique physiological functions,[21,22] and it could be promising to conjugate NIR-II fluorophores to specific hormones for molecular imaging. In this work, luteinizing hormone (LH) was adopted as a model case to target mouse ovaries and achieve efficient targeted imaging of live animals with a high penetration depth. LH belongs to the cystine-knot glycoprotein hormone family[23] that also includes follicle stimulating hormone (FSH), thyroid stimulating hormone (TSH), and human chorionic gonadotropin (hCG). Bioconjugation between different hormones/antibodies and fluorophores with nonoverlapping emission could allow multicolor molecular imaging of different hormone receptors in the NIR-II region, which could be an important advance in the field of NIR-II molecular imaging.

We used a new NIR-II fluorophore infrared fluorene 3,4-ethyl-enedioxythiophene polyethylene-glycol carboxyl (IR-FEPC) (nine times brighter than CH1055PEG)[19] conjugated to hCG for specific imaging of LH receptors in three stages of ovary (immature untreated, equine chorionic gonadotropin (eCG)-treated, and eCG/hCG-treated ovary). This new bioconjugate together with NIR-II one-photon confocal technique facilitated 3D imaging of formalin fixed ovaries without tissue clearing techniques with a ≈900 μm imaging depth. In addition, we imaged LH receptors expressed in the uterus following

gonadotropin treatment. 3D confocal microscopy during three different ovarian stages distinguished theca, granulosa, and luteal cell enriched sub-regions. By using different bioconjugates with distinct emission spectra in the NIR-II sub-windows (a NIR-IIa fluorophore with 1100–1300 nm emission and a NIR-IIb fluorophore with over 1500 nm emission), we performed simultaneous imaging of receptors for two ligands (LH/hCG and FSH) that are important for gonadal development as a demonstration of multicolor molecular imaging in the NIR-II window.

Recombinant hCG was covalently conjugated to a newly developed bright IR-FEPC fluorophore (Figure 1a)[20,24] (see the Supporting Information for more conjugation detail). The UV–vis–NIR absorption spectrum of the IR-FEPC aqueous solution exhibited an absorption peak ≈782 nm, whereas the fluorescence emission spectrum showed a main emission peak at 1,053 nm and displayed a large Stokes shift of ≈400 nm (Figure 1b).[25,26] Quantum yield (QY) of IR-FEPC in the aqueous solution was 0.26–2.6% considering discrepancies in the reported QY of the IR26 reference fluorophore (see Table SI of the Supporting Information for more details),[27] among the highest of water-soluble NIR-II dyes with carboxyl functional groups.[19,28] After optimizing the conjugation reaction with different ratios of hCG and fluorophore in several reaction buffers, we performed polyacrylamide gel electrophoresis to confirm the high purity of hCG@IR-FEPC conjugates (Figure S1, Supporting Information).

We initially sought to track the performance of the administrated bioconjugate at the cellular level. We obtained ovarian lysates from immature mice containing mainly theca cells (TC), punctured large preovulatory follicles of immature mice pretreated with equine chorionic gonadotropin (eCG) containing mature granulosa cells (GC), as well as lysates from immature mice pretreated with eCG followed by hCG for 3 d for the enrichment of luteal cells (LC).[29] Lysates of these cells and the LH receptor-deficient U87 glioblastoma cells were printed on plasmonic, NIR fluorescence-enhancing gold (pGOLD) slide[30] to form the reverse phase microarrays before incubation with hCG@IR-FEPC. The assay results showed that TC, mature GC and LC had positive signals derived from the hCG binding receptors (Figure 1c). We also evaluated the binding affinity by using this assay method. A Scatchard plot was obtained by testing the fluorescence intensity of mature GC lysate with graded concentrations of hCG@IR-FEPC, giving a K_d value ≈43×10^{-9} M (Figure 1d). Using this cell line (Figure 1e), we confirmed that fluorescent IR-FEPC labeling of hCG did not interfere with the hormone's binding specificity.

To obtain high-resolution NIR-II imaging, we developed a home-built NIR-II confocal microscope (Figure 2a).[31,32] In brief, a collimated NIR 785 nm laser excitation beam was allowed to pass the excitation filter and the back aperture of the objective lens before it reached a sharp focus at a certain focal plane inside the volume of a sample (two pairs of lenses were used for expanding beam size). Fluorescence emission from the mice/tissue passed back through the same objective in the opposite direction. A short-pass dichroic filter was placed behind the objective to reject the excitation beam.[33] The path of the fluorescence (pink beam in Figure 2a) was then focused onto the pinhole by a tube lens, with the sample focal plane and the pinhole plane at a pair of conjugate planes. Fluorescence was allowed to pass through an emission filter and focused onto a NIR photomultiplier diode

(PMT, sensitive to photons up to 1700 nm) by a camera lens. Like a regular confocal microscope, there were three conjugate planes including the front focal plane of the objective, the pinhole plane and the plane of the active area of the PMT. Out-of-focus signal from the sample was rejected by the pinhole and thus could not to form an image on the photodetector. The specialty of our confocal system was the use of a NIR excitation laser, the IR compatible optical components including the objective and the NIR PMT.

We next performed imaging of LH receptors in ovarian follicles and the corpora lutea of adult female mice in vivo based on hCG@IR-FEPC (Figure 2b,c). Upon tail-vein administration of hCG@IR-FEPC into adult female mice, we observed initial accumulation of nonspecific signals in the kidney and liver. Signals appeared in the ovary and reached the highest levels at 1–2 h (Video S1, Supporting Information; Figure 2d). The observed signals of both the ovary and uterus encouraged us to investigate the gonadal development (Figure 2e, see the next section). To address whether free IR-FEPC could be independently absorbed by ovary, we performed a control experiment with the injection of a similar dose of nonconjugated IR-FEPC. No ovary signal was found in the NIR-II imaging of the mouse body, suggesting specificity of ovarian targeting of hCG@IR-FEPC (Figure S2, Supporting Information). With the bright IR-FEPC, we were able to use a one-photon confocal microscope to obtain the 3D structure of the ovary after formalin fixation in a layer-by-layer fashion. We detected bright signals in theca (white arrows) and granulosa cells (black arrows) inside individual follicles together with the corpora lutea (blue arrows) (Figure 2f,g; Video S2, Supporting Information). The 3D confocal NIR-II imaging depth for fixed ovaries was hundreds of micrometers (Figure 2h).

Next, we performed 3D imaging of LH receptors in ovarian follicles at three different stages of ovary development. In immature female mice at age of 23 d, administrations of hCG@IR-FEPC led to clear signals in the immature untreated, eCG-treated, and eCG/hCG-treated ovaries, respectively (Figure S3, Supporting Information). We named the three stages of the ovary as immature untreated ovary (1), eCG-treated ovary (2), and eCG/hCG-treated ovary (3). Previous studies demonstrated that FSH treatment increased the LH receptors in mature granulosa cells of preovulatory follicles.[29] Some immature mice were pretreated with eCG before the injection of hCG@IR-FEPC to develop the eCG-treated ovary. As shown in Figure S4b (Supporting Information), strong NIR-II signals were found in the eCG-treated ovary. We then induced the formation of corpora lutea by injecting an ovulatory dose of hCG into eCG-primed immature mice. Three days after hCG treatment, the animals were injected with a conjugated fluorophore. As shown in Figure S4c (Supporting Information), strong signals were found in the eCG/hCG-treated ovary with the predominant binding of hCG@IR-FEPC to the corpora lutea. For all experiments, the injection of free IR-FEPC led to negligible signals in the ovary (Figure S5, Supporting Information), again confirming binding of hCG@IR-FEPC to specific target cells. Because eCG treatment increases follicle sizes to the large preovulatory follicles, imaging signal of the eCG-treated ovary is higher than the immature untreated one (Figure 3a). Compared with 2D whole body imaging (Figure 3b), confocal analyses clearly indicated strong signals in the theca layer surrounding the follicles, the mature granulosa of preovulatory follicles, and the luteal cell of the corpus luteum (Figure S6, Supporting Information; Figure 3c,d).

Confocal analyses also indicated that three stages of ovary with a 900 μm depth imaging could be achieved at micrometers resolution (Videos S3–S5, Supporting Information, with the 18 μm "*z*" interval between each layers). For all three ovarian stages, theca layers appeared to surround the follicles. For immature untreated ovary, the secondary follicles had negligible LH receptors on immature GC compared to the eCG treated ovary. For eCG-treated ovary, there were theca cells in the secondary follicles plus mature granulosa cells in preovulatory follicles showing strong LH receptor signals. For the eCG/hCG-treated ovary, there was a newly formed corpus luteum with existing follicles (secondary and preovulatory ones), and the major signals were found in the corpora lutea and follicles (see Videos S6–S8 of the Supporting Information for 3D reconstructed images).

We then aimed to uncover the hCG-receptor evolution in the uterus at different stages of ovary development. After injecting hCG@IR-FEPC to immature female mice pretreated with eCG for 48 h, we found strong NIR-II signals in the uterus (Figure 3a; Figure S4b, Supporting Information). Confocal imaging of NIR-II signals further demonstrated higher NIR-II signals in the myometrium and lower signals in the endometrium (Figure S7, Supporting Information). In contrast, NIR-II signals were not found in the uterus of immature mice pretreated with eCG (48 h) followed by hCG (72 h) (Figure S4c, Supporting Information), which indicated that LH receptors were present in the uterus of the proliferative but not the secretory phase.

In an attempt to achieve multicolor NIR-II imaging with deep tissue penetration and high resolution, two-color simultaneous imaging of ovarian LH/hCG and FSH receptors was performed using the home-built confocal set-up. FSH and hCG are two gonadotropins that act simultaneously to affect ovarian follicle maturation.[29] Benefitting from the bioconjugation of hCG and FSH to different fluorophores with nonoverlapping emission spectra in the NIR-II window, we were able to do simultaneous imaging of the receptors for both ligands, useful to probing gonadal development. Figure 4a shows the photoluminescence spectra of the two designed conjugates, hCG@IR-FEPC and FSH@lead sulfide (PbS) nanocrystal, with the fluorophores possessing nonoverlap emission at the NIR-IIa and -IIb regions, respectively. In vitro binding specificity showed that the hCG probe can bind to TC and GC lysates, whereas the FSH probe can only bind to GC lysates (Figure 4b). Cell imaging also showed successful conjugation between PbS nanocrystals and FSH (Figure 4c). From the in vivo two-color imaging of adult female mice after administration of two conjugates, the ovary could be seen in both hCG@IR-FEPC and FSH@PbS channels, which indicated successful binding of two separate receptors (Video S9 and Figure S8, Supporting Information; Figure 4d,e).

Imaging using 1100 nm long pass maximized detecting total fluorescence signals of IR-FEPC. We obtained much clearer imaging by changing 1100 nm long pass filter to 1200 nm long pass (Figure S8a, Supporting Information), showing more detailed structures than with the 1100 nm channel owing to further reduced photon scattering. From ex vivo two-color imaging of ovary (removal from mice) with both TC and mature GC, simultaneous imaging of receptors for both ligands (hCG and FSH) was achieved (Figure 4f; Figure S9, Supporting Information). hCG@IR-FEPC labeled both the TC and GC layers, whereas the FSH@PbS only stained the GC layer (a comparison experiment by FSH@IR-FEPC and FSH@PbS was

additionally performed and the images were listed in Figure S10 of the Supporting Information). In addition to the magnified whole body imaging of FSH@PbS stained ovary (Figure 4g), 2D and 3D confocal imaging of the FSH@PbS stained ovary showed detailed follicle and vessel structures with ≈1125 μm depth and micrometers resolution (Figure 4h–j; Figure S11, Supporting Information). Note that most organic based NIR-II fluorophores including the recent D–A–D dyes suffer from low quantum yields due to nonradiative electron/hole recombination in low energy-gap molecules. As a result, we have not yet succeeded in synthesizing an efficient NIR-IIb (over 1500 nm emission) organic fluorophore to replace PbS quantum dots. This will require future efforts in this field.

Epifluorescence imaging in the NIR-II window is limited to 3D structural features projected onto a 2D plane. In contrast, confocal imaging collects signals from a small probe volume at the focus while rejecting out-of-focus signals and allows 3D imaging in a layer-by-layer fashion by scanning the laser focal point in the *x–y–z* directions.[34–37] A requirement for confocal molecular imaging is highly biospecific binding of fluoro-phores.[38–42] Targeted molecular imaging in NIR-II allows for better sensitivity and specificity with little nonspecific background staining.[41,43,44]

3D fluorescence imaging of biological samples has relied on mechanical sectioning, optical sectioning and optical clearing treatments to achieve sufficient imaging penetration depth with high spatial resolution.[15,45] Although 3D ovary imaging was achieved by CLARITY clearing techniques, it takes a long time to complete immunological histological chemistry (IHC) because it requires long steps in a hydrogel.[16,46] The present in vivo molecular imaging in the mouse body is a time-saving way for imaging intact tissues, and the 3D imaging of the ovary can be obtained without any pre-/postclearing or IHC step. In addition, we also anticipate that two-photon imaging, photoacoustic imaging, and afterglow imaging in NIR-II window could further improve the penetration depth, signal to background ratio, and contrast resolution of noninvasive optical imaging techniques.[47–50]

Our findings showing high levels of hCG@IR-FEPC binding to the eCG-primed uterus are consistent with the role of LH/hCG in regulating uterine functions and provides future in vivo monitoring of uterine LH receptors under different physiological states.[51] The present imaging approach also allows imaging of the LH receptor in normal Leydig cells (Figure S12, Supporting Information) and could facilitate the monitoring of disease progression of Leydig cell tumors. Based on the present strategy, conjugation of the NIR-II fluorophore to the paralogous TSH could allow imaging of specific target cells expressing TSH receptors (thyroid nodules) (see preliminary data in Figure S13 of the Supporting Information). Further refinement of the present NIR-II fluorophore conjugation approach could pave the way to the live imaging of receptors for diverse peptide and protein hormones in their target tissues.[52,53]

In conclusion, 3D NIR-II molecular imaging was achieved in a model of mouse ovaries with great penetration depth and micrometers spatial resolution through both high-performance hCG@IR-FEPC conjugate and a home-built NIR-II confocal set-up. With the help of high-resolution confocal microscopy, three different ovary development stages with theca, granulose, and luteal enriched cells were distinguished. We envisage that NIR-II

fluorescence microscopy will become a powerful imaging technique for deep tissue molecular imaging, providing a new solution for visualizing tissue structures and simultaneously allowing molecular phenotyping in a large tissue volume. Our studies also open up more and deeper nonoverlapping molecular imaging channels for complex biological systems beyond the traditional visible NIR-I range, which could increase imaging multiplicity and capability of molecular imaging based on fluorescence techniques.

Supplementary Material

Refer to Web version on PubMed Central for supplementary material.

Acknowledgments

This work was partially supported by National Institutes of Health NIH DP1-NS-105737, the Deng family gift, the Office of Science (BER), NCI Cancer Center Nanotechnology Excellence Grant (CCNE-TR). This study was also supported by grants from the Calbrain Program and the National Institutes of HealthRO1 HL127113-01A1 (to H.D.). Y.L. acknowledges financial support from Shenzhen Key Lab Funding Grant ZDSYS201505291525382 and the Shenzhen Peacock Program Grant KQTD20140630160825828. S.Z. thanks Dr. Xue Zhang in Jilin University for scheme designing. The vertebrate animal handling was performed under the Stanford University's Administrative Panel on Laboratory Animal Care (APLAC). The animals were housed in Research Animal Facility (RAF II, Room 053) under the approved animal protocols (11253 and 21556).

References

1. Hong G, Antaris AL, Dai H. Nat. Biomed. Eng. 2017; 1:0010.
2. Yi H, Ghosh D, Ham M-H, Qi J, Barone PW, Strano MS, Belcher AM. Nano Lett. 2012; 12:1176. [PubMed: 22268625]
3. Ishizawa T, Fukushima N, Shibahara J, Masuda K, Tamura S, Aoki T, Hasegawa K, Beck Y, Fukayama M, Kokudo N. Cancer. 2009; 115:2491. [PubMed: 19326450]
4. Hong G, Zou Y, Antaris AL, Diao S, Wu D, Cheng K, Zhang X, Chen C, Liu B, He Y. Nat. Commun. 2014; 5:4206. [PubMed: 24947309]
5. Franke D, Harris DK, Chen O, Bruns OT, Carr JA, Wilson MW, Bawendi MG. Nat. Commun. 2016; 7:12749. [PubMed: 27834371]
6. Zhang Y, Hong G, Zhang Y, Chen G, Li F, Dai H, Wang Q. ACS Nano. 2012; 6:3695. [PubMed: 22515909]
7. Zhang X, Wang H, Antaris AL, Li L, Diao S, Ma R, Nguyen A, Hong G, Ma Z, Wang J, Zhu S, Castellano JM, Coray T, Liang Y, Luo J, Dai H. Adv. Mater. 2016; 28:6872. [PubMed: 27253071]
8. Feng W, Han C, Li F. Adv. Mater. 2013; 25:5287. [PubMed: 23982981]
9. Zhong Y, Ma Z, Zhu S, Yue J, Zhang M, Antaris AL, Yuan J, Cui R, Wan H, Zhou Y, Wang W, Huang NF, Luo J, Hu Z, Dai H. Nat. Commun. 2017; 8:737. [PubMed: 28963467]
10. Diao S, Blackburn JL, Hong G, Antaris AL, Chang J, Wu JZ, Zhang B, Cheng K, Kuo CJ, Dai H. Angew. Chem., Int. Ed. 2015; 54:14758.
11. Tao Z, Hong G, Shinji C, Chen C, Diao S, Antaris AL, Zhang B, Zou Y, Dai H. Angew. Chem., Int. Ed. 2013; 125:13240.
12. Starosolski Z, Bhavane R, Ghaghada KB, Vasudevan SA, Kaay A, Annapragada A. PLoS One. 2017; 12:e0187563. [PubMed: 29121078]
13. Welsher K, Liu Z, Sherlock SP, Robinson JT, Chen Z, Daranciang D, Dai H. Nat. Nanotechnol. 2009; 4:773. [PubMed: 19893526]
14. Welsher K, Sherlock SP, Dai H. Proc. Natl. Acad. Sci. USA. 2011; 108:8943. [PubMed: 21576494]
15. Li AA, Gong H, Zhang B, Wang QD, Yan C, Wu JP, Liu QA, Zeng SQ, Luo QM. Science. 2010; 330:1404. [PubMed: 21051596]

16. Chung K, Wallace J, Kim SY, Kalyanasundaram S, Andalman AS, Davidson TJ, Mirzabekov JJ, Zalocusky KA, Mattis J, Denisin AK, Pak S, Bernstein H, Ramakrishnan C, Grosenick L, Gradinaru V, Deisseroth K. Nature. 2013; 497:332. [PubMed: 23575631]
17. Yang B, Treweek JB, Kulkarni RP, Deverman BE, Chen CK, Lubeck E, Shah S, Cai L, Gradinaru V. Cef/. 2014; 158:945.
18. Feng Y, Zhu S, Antaris AL, Chen H, Xiao Y, Lu X, Jiang L, Diao S, Yu K, Wang Y, Herraiz S, Yue J, Hong X, Hong G, Cheng Z, Dai H, Hsueh AJ. Chem. Sci. 2017; 8:3703. [PubMed: 28626555]
19. Antaris AL, Chen H, Cheng K, Sun Y, Hong G, Qu C, Diao S, Deng Z, Hu X, Zhang B, Zhang X, Yaghi OK, Alamparambil ZR, Hong X, Cheng Z, Dai H. Nat. Mater. 2016; 15:235. [PubMed: 26595119]
20. Zhu S, Yang Q, Antaris AL, Yue J, Ma Z, Wang H, Huang W, Wan H, Wang J, Diao S, Zhang B, Li X, Zhong Y, Yu K, Hong G, Luo J, Liang Y, Dai H. Proc. Natl. Acad. Sci. USA. 2017; 114:962. [PubMed: 28096386]
21. Ben-Shlomo I, Yu Hsu S, Rauch R, Kowalski HW, Hsueh AJ. Sci. STKE. 2003; 2003:RE9. [PubMed: 12815191]
22. Zhu G, Niu G, Chen X. Bioconjug. Chem. 2015; 26:2186. [PubMed: 26083153]
23. Vitt UA, Hsu SY, Hsueh AJ. Mol. Endocrinol. 2001; 15:681. [PubMed: 11328851]
24. Yang Q, Ma Z, Wang H, Zhou B, Zhu S, Zhong Y, Wang J, Wan H, Antaris A, Ma R, Zhang X, Yang J, Zhang X, Sun H, Liu W, Liang Y, Dai H. Adv. Mater. 2017; 29:1605497.
25. Pittet MJ, Weissleder R. Cell. 2011; 147:983. [PubMed: 22118457]
26. Sun Y, Qu C, Chen H, He M, Tang C, Shou K, Hong S, Yang M, Jiang Y, Ding B, Xiao Y, Xing L, Hong X, Cheng Z. Chem. Sci. 2016; 7:6203.
27. Han S, Qin X, An Z, Zhu Y, Liang L, Han Y, Huang W, Liu X. Nat. Commun. 2016; 7:13059. [PubMed: 27698348]
28. Feng Y, Zhu S, Antaris AL, Chen H, Xiao Y, Lu X, Jiang L, Diao S, Yu K, Wang Y, Herraiz S, Yue J, Hong X, Hong G, Cheng Z, Dai H, Hsueh AJ. Chem. Sci. 2017; 8:3703. [PubMed: 28626555]
29. Hsueh AJ, Adashi EY, Jones PB, Welsh TH Jr. Endocr. Rev. 1984; 5:76. [PubMed: 6142819]
30. Zhang B, Pinsky BA, Ananta JS, Zhao S, Arulkumar S, Wan H, Sahoo MK, Abeynayake J, Waggoner JJ, Hopes C, Tang M, Dai H. Nat. Med. 2017; 23:548. [PubMed: 28263312]
31. Nichols AJ, Evans CL. J. Vis. Exp. 2011; 56:3252.
32. Wilson, T. Confocal Microscopy. Vol. 426. Academic Press; 1990. p. 1
33. D'Aleo A, Bourdolle A, Brustlein S, Fauquier T, Grichine A, Duperray A, Baldeck PL, Andraud C, Brasselet S, Maury O. Angew. Chem., Int. Ed. 2012; 51:6622.
34. Piyawattanametha W, Ra H, Qiu Z, Friedland S, Liu JT, Loewke K, Kino GS, Solgaard O, Wang TD, Mandella MJ, Contag CH. J. Biomed. Opt. 2012; 17:021102. [PubMed: 22463020]
35. Wang K, Wang Q, Luo Q, Yang X. Opt. Exp. 2015; 23:12669.
36. Glaser AK, Reder NP, Chen Y, McCarty EF, Yin C, Wei L, Wang Y, True LD, Liu JTC. Nat. Biomed. Eng. 2017; 1:0084.
37. Gu X, Zhao E, Zhao T, Kang M, Gui C, Lam JW, Du S, Loy MM, Tang BZ. Adv. Mater. 2016; 28:5064. [PubMed: 27135807]
38. Chen Y, Chen H, Shi J. Adv. Mater. 2013; 25:3144. [PubMed: 23681931]
39. Ge J, Jia Q, Liu W, Guo L, Liu Q, Lan M, Zhang H, Meng X, Wang P. Adv. Mater. 2015; 27:4169. [PubMed: 26045099]
40. Zhang X, Wang H, Wang H, Zhang Q, Xie J, Tian Y, Wang J, Xie Y. Adv. Mater. 2014; 26:4438. [PubMed: 24811730]
41. Wu C, Chiu DT. Angew. Chem., Int. Ed. 2013; 52:3086.
42. Kong B, Zhu A, Ding C, Zhao X, Li B, Tian Y. Adv. Mater. 2012; 24:5844. [PubMed: 22933395]
43. Jayapaul J, Arns S, Bunker M, Weiler M, Rutherford S, Comba P, Kiessling F. Nano Res. 2016; 9:1319. [PubMed: 27738498]
44. Yang Y, Liu J, Sun X, Feng L, Zhu W, Liu Z, Chen M. Nano Res. 2015; 9:139.
45. Lein ES, Hawrylycz MJ, Ao N, Ayres M, Bensinger A, Bernard A, Boe AF, Boguski MS, Brockway KS, Byrnes EJ. Nature. 2006; 445:168. [PubMed: 17151600]

46. Feng Y, Cui P, Lu X, Hsueh B, Moller Billig F, Zarnescu Yanez L, Tomer R, Boerboom D, Carmeliet P, Deisseroth K, Hsueh AJ. Sci. Rep. 2017; 7:44810. [PubMed: 28333125]
47. Lyu Y, Cui D, Sun H, Miao Y, Duan H, Pu K. Angew. Chem., Int. Ed. 2017; 56:9155.
48. Jiang Y, Upputuri PK, Xie C, Lyu Y, Zhang L, Xiong Q, Pramanik M, Pu K. Nano Lett. 2017; 17:4964. [PubMed: 28654292]
49. Miao Q, Xie C, Zhen X, Lyu Y, Duan H, Liu X, Jokerst JV, Pu K. Nat. Biotechnol. 2017; 35:1102. [PubMed: 29035373]
50. Jiang Y, Pu K. Small. 2017; 13:1700710.
51. Ambrus G, Rao CV. Endocrinology. 1994; 135:2772. [PubMed: 7988470]
52. Zhang Z, Wang J, Chen C. Adv. Mater. 2013; 25:3869. [PubMed: 24048973]
53. Hyun H, Owens EA, Wada H, Levitz A, Park G, Park MH, Frangioni JV, Henary M, Choi HS. Angew. Chem., Int. Ed. 2015; 54:8648.

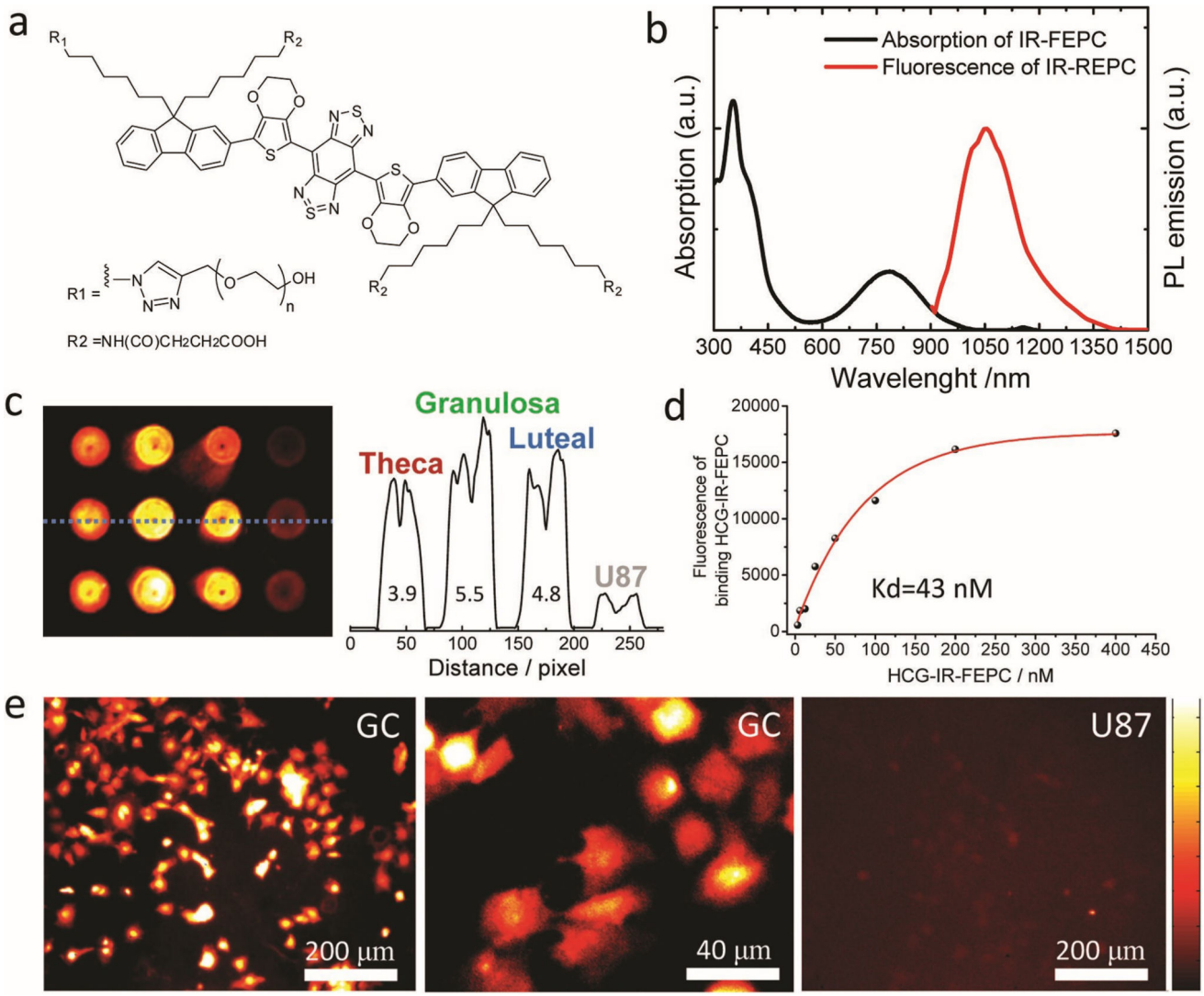

Figure 1.

Conjugation of hCG to the IR-FEPC fluorophore: binding of the conjugates to LH receptors in vitro. a) Chemical structure of IR-FEPC with a donor–acceptor–donor architecture pertaining PEG chain and carboxyl groups for biocompatibility and bioconjugation, respectively. b) Absorption and emission spectra of IR-FEPC. c) Binding of hCG@IR-FEPC to the ovarian lysate but not human glioblastoma U87MG cells. The insert values are positive/negative ratios. d) Scatchard plot of hCG@IR-FEPC binding to ovarian cell lysates; it should be noted that the obtained K_d value is higher than the actual one due the detection limit of the method. e) The mature GC incubated with 500×10^{-9} M hCG@IR-FEPC for 4 h displayed bright NIR-II signals compared with negligible signals from the U87-MG glioblastoma cells. The imaging was obtained by an 808 nm laser and 1100 nm long-pass filter and the background scale of U87 image was lowered to visualize the cells clearly.

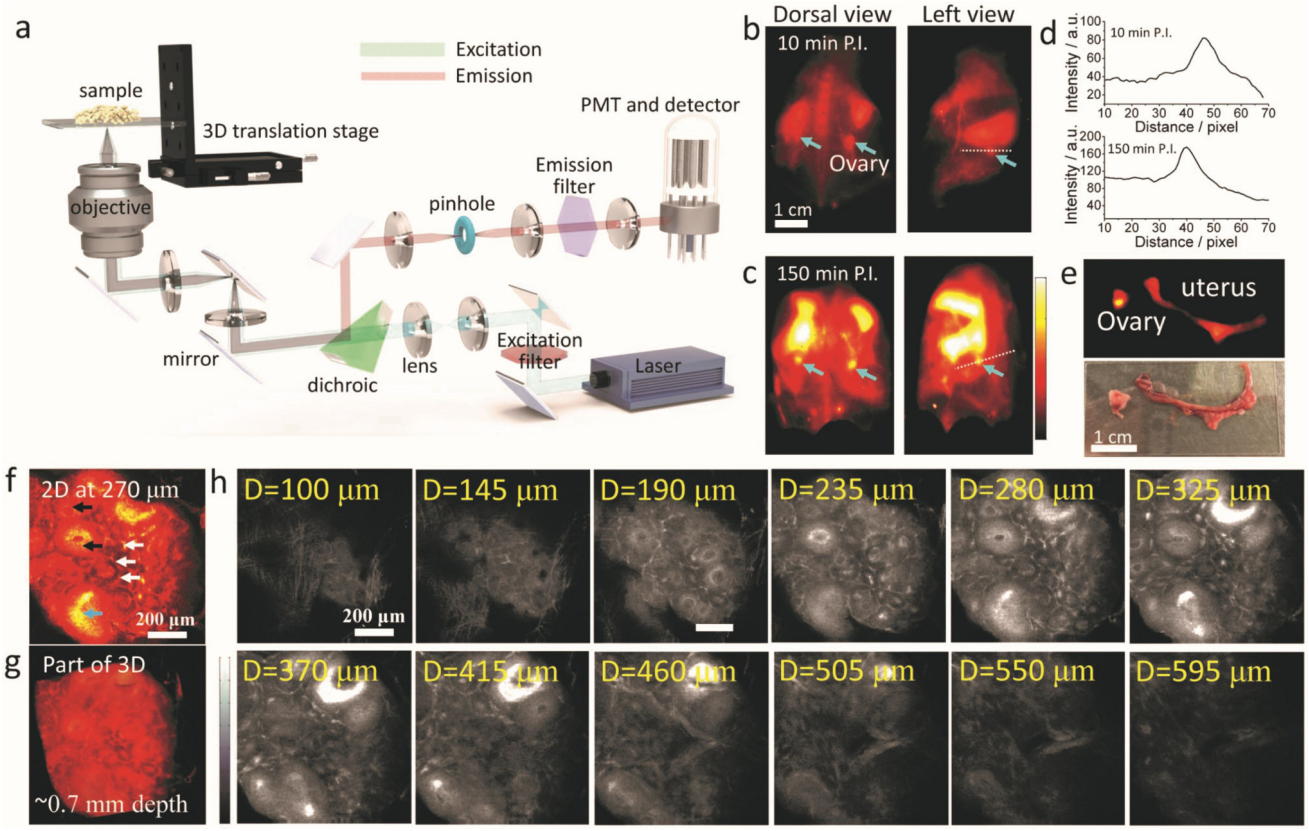

Figure 2.

NIR-II confocal set-up and NIR-II imaging of ovarian follicles using hCG@IR-FEPC in adult female mice. a) A simplified optical diagram of the stage-scanning NIR-II fluorescence confocal microscopy. b,c) hCG@IR-FEPC was injected into the tail vein of an adult female mouse before NIR-II imaging at 10 and 150 min post-injection (P.I.) time points. Side view images are shown to focus on one ovary and two ovaries can be observed by dorsal view images. d) Cross-section profile (drawn dashed lines in b–c) shows signal-to-normal tissue ratio (SNR) of ovary as 2.6 and 2.7 respectively. e) Ex vivo imaging of the ovary and uterus by NIR-II (upper) and daylight (nether). f,g) Confocal image of the partial ovary shows bright signals in theca (white arrows) and granulosa cells (black arrows) inside individual follicles together with corpora lutea (blue arrows). h) Layer-by-layer confocal scanning of the partial ovary. For confocal imaging the samples were mounted on coverglass and immersed in glycerol. The scanned depth was corrected considering the refractive index difference of air and ovary samples.

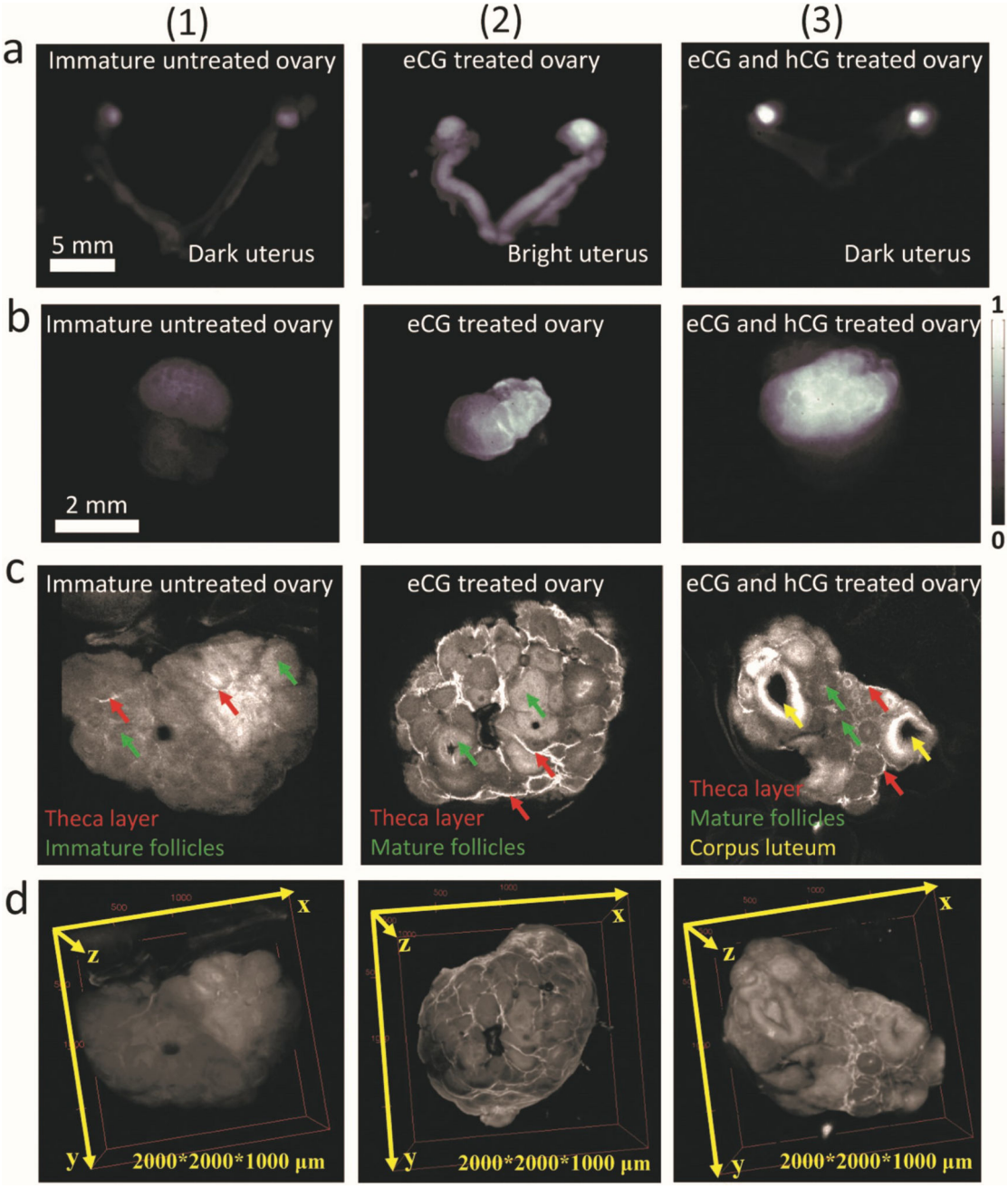

Figure 3.

NIR-II imaging of the theca layer in ovarian follicles, mature granulosa cells of preovulatory follicles and corpora lutea using hCG@IR-FEPC. We named the three stages of the ovary as immature untreated ovary (1), eCG-treated ovary (2), and eCG/hCG-treated ovary (3). a) A 2.5× magnification whole body imaging of the three ovaries after removal from the body with the uterus and imaging signal of the immature untreated ovary is less than the eCG-treated and eCG/hCG-treated ovary. Note the NIR-II signals in the uterus of eCG-pretreated but not in untreated and eCG/hCG-treated animals. b) The 15× magnification whole body imaging of the separate ovary after removal from the body with lower resolution compared

with confocal imaging. c,d) 2D and 3D confocal imaging of the ovary after removal from the body showed strong signals in the theca layer of the follicles, mature granulosa cells of the follicles of eCG pretreated mice, and corpora lutea of the eCG/hCG pretreated mice.

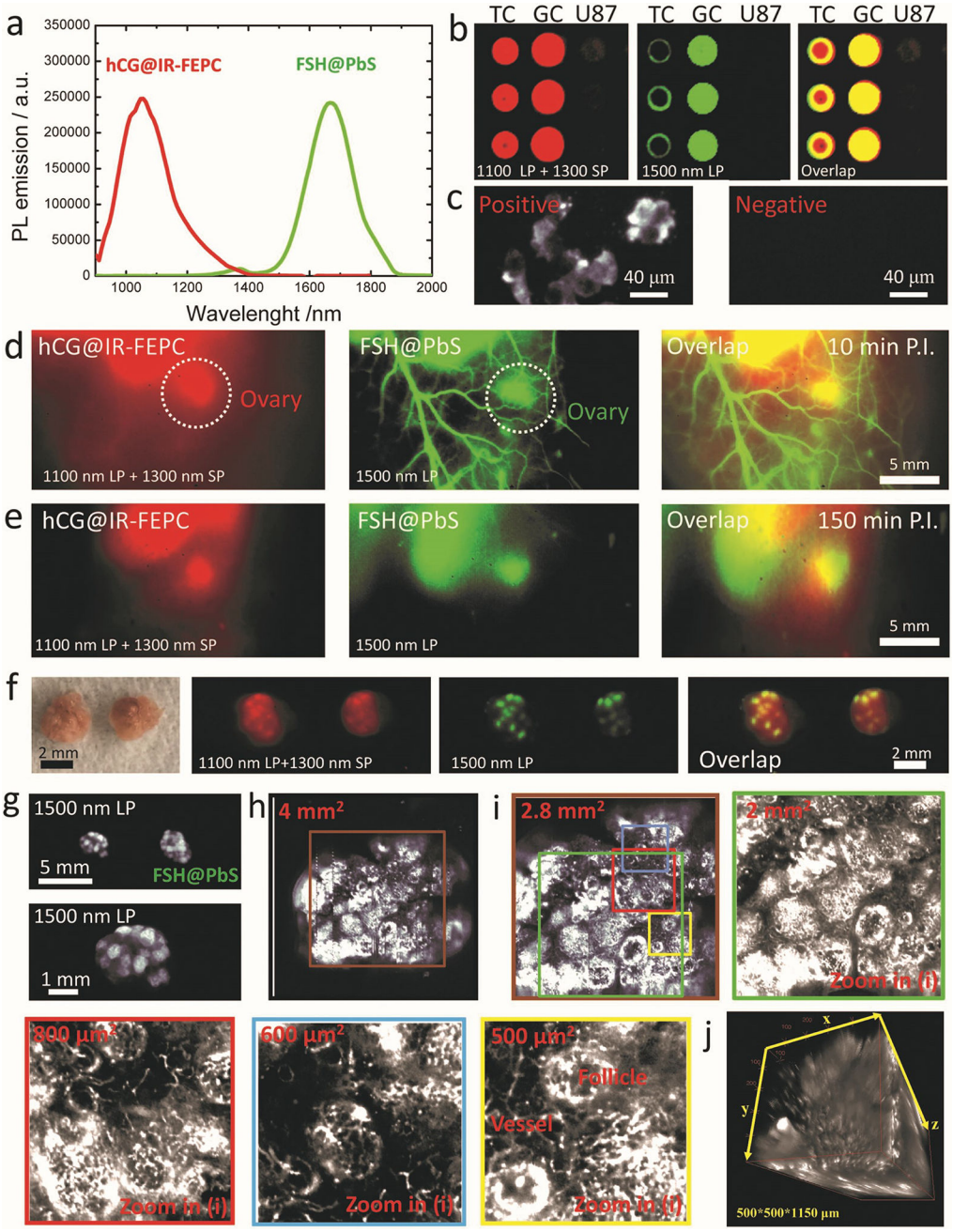

Figure 4.

NIR-II two-color simultaneous imaging of ovarian LH/hCC and FSH receptors. a) Photoluminescence spectra of hCG@IR-FEPC and FSH@PbS. b) Analysis of cell lysate binding using conjugates. TC, GC, and U87 cell lysates were printed on plasmonic fluorescence-enhancing pGOLD slides to test binding specificity of the conjugates. The slide was scanned by a 10× magnification NIR-II set-up with 808 nm excitation and 1100 nm long-pass (LP) plus 1300 nm short pass (SP) emission filter for IR-FEPC channel and 1500 nm LP filter for PbS channel. c) Positive (mature GC) and negative (U87) cell imaging of FSH@PbS. d,e) In vivo two-color imaging of the adult female ovary at 10 and 150 min post

injection time points. The 1100 nm long pass was chosen to maximize signal intensity and we could still obtain clearer imaging by changing 1100 long pass filter to the 1200 one (Figure S8a, Supporting Information): Figure S8a of the Supporting Information used 1200 nm long pass channel and showed enhanced detailed structures compared with the 1100 nm channel. f) Ex vivo two-color imaging of the adult female ovary. hCG@IR-FEPC labeled both the TC layer and GC layer, whereas the FSH@PbS only stained the GC layer. g) The 2.5× and 15× magnification whole body imaging of the FSH@PbS-stained ovary. h,i) 2D confocal imaging of the FSH@PbS-stained ovary after removal from the body; it showed strong signals in all follicles with mature granulosa cells. The magnified figures showed clear signals in follicles and vessels. j) 3D reconstruction confocal imaging of the FSH@PbS stained ovary with 1150 μm depth.